CityU Scholars

Tuning the Bandgap of Photo-Sensitive Polydopamine/Ag3PO4/Graphene Oxide Coating for Rapid, Noninvasive Disinfection of Implants

Xie, Xianzhou; Mao, Congyang; Liu, Xiangmei; Tan, Lei; Cui, Zhenduo; Yang, Xianjin; Zhu, Shengli; Li, Zhaoyang; Yuan, Xubo; Zheng, Yufeng; Yeung, Kelvin Wai Kwok; Chu, Paul K.; Wu, Shuilin

Document Version:
Final Published version, also known as Publisher's PDF, Publisher's Final version or Version of Record

License:
Other

Publication record in CityU Scholars:
Go to record

Published version (DOI):
10.1021/acscentsci.8b00177

Tuning the Bandgap of Photo-Sensitive Polydopamine/Ag₃PO₄/ Graphene Oxide Coating for Rapid, Noninvasive Disinfection of Implants

Xianzhou Xie,[†,‡] Congyang Mao,[†,‡] Xiangmei Liu,[‡] Lei Tan,[‡] Zhenduo Cui,[†] Xianjin Yang,[†] Shengli Zhu,[†] Zhaoyang Li,[†] Xubo Yuan,[†] Yufeng Zheng,[§] Kelvin Wai Kwok Yeung,[∥] Paul K. Chu,[⊥] and Shuilin Wu*,[†,‡]

[†]School of Materials Science & Engineering, Tianjin University, Tianjin 300072, China

[‡]Hubei Collaborative Innovation Center for Advanced Organic Chemical Materials, Ministry-of-Education Key Laboratory for the Green Preparation and Application of Functional Materials, Hubei Key Laboratory of Polymer Materials, School of Materials Science & Engineering, Hubei University, Wuhan 430062, China

[§]State Key Laboratory for Turbulence and Complex System and Department of Materials Science and Engineering, College of Engineering, Peking University, Beijing 100871, China

[∥]Department of Orthopaedics & Traumatology, Li KaShing Faculty of Medicine, The University of Hong Kong, Pokfulam, Hong Kong 999077, China

[⊥]Department of Physics and Department of Materials Science and Engineering, City University of Hong Kong, Tat Chee Avenue, Kowloon, Hong Kong 999077, China

S *Supporting Information*

ABSTRACT: Bacterial infection and associated complications are threats to human health especially when biofilms form on biomedical devices and artificial implants. Herein, a hybrid polydopamine (PDA)/Ag₃PO₄/graphene oxide (GO) coating is designed and constructed to achieve rapid bacteria killing and eliminate biofilms in situ. By varying the amount of GO in the hybrid coating, the bandgap can be tuned from 2.52 to 2.0 eV so that irradiation with 660 nm visible light produces bacteria-killing effects synergistically in concert with reactive oxygen species (ROS). GO regulates the release rate of Ag⁺ to minimize the cytotoxicity while maintaining high antimicrobial activity, and a smaller particle size enhances the yield of ROS. After irradiation with 660 nm visible light for 15 min, the antimicrobial rates of the PDA/Ag₃PO₄/GO hybrid coating against *Escherichia coli* and *Staphylococcus aureus* are 99.53% and 99.66%, respectively. In addition, this hybrid coating can maintain a repeatable and sustained antibacterial efficacy. The released Ag⁺ and photocatalytic Ag₃PO₄ produce synergistic antimicrobial effects in which the ROS increases the permeability of the bacterial membranes to increase the probability of Ag⁺ to enter the cells to kill them together with ROS synergistically.
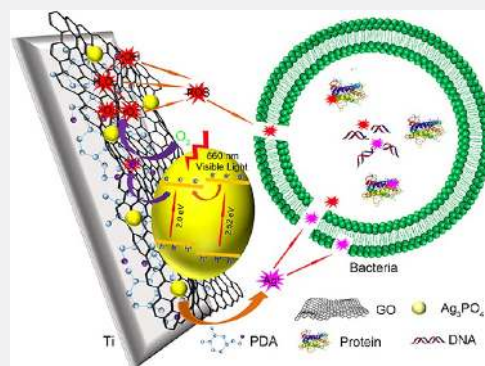
INTRODUCTION

Artificial implants for surgical repair or reconstruction of damaged tissues are prone to bacterial infection because the interfaces between the implants and surrounding tissues provide the space for bacterial growth.[1] To solve this problem, antimicrobial agents are introduced,[2,3] but traditional treatment usually requires a long antimicrobial cycle which in turn results in the development of drug-resistant bacteria and prolongs patient suffering.[4−7] Hence, it is important to develop a novel, instantaneous, and efficient antimicrobial method. Reactive oxygen species (ROS) such as peroxide, superoxide, hydroxyl radicals, and singlet oxygen possess rapid bacteria-killing ability,[8−10] because they can damage the DNA, proteins, and membranes of bacteria without producing drug-resistant bacteria.[11,12] Furthermore, ROS can be generated instanta-

neously to kill bacteria quickly in a short antimicrobial cycle.[13] ROS are normally produced by the combination of O₂ with escaping electrons from various photosensitive materials under irradiation with photons of the appropriate wavelength,[14−16] but in the complex in vivo environment, production of ROS is often limited by the lack of oxygen and that only light with a certain wavelength can penetrate skin tissues.

Ag₃PO₄ has remarkable photocatalytic capability[17,18] and can produce a large amount of ROS during light exposure.[19,20] Ag₃PO₄ is soluble in water to release Ag⁺,[21] and so bacteria can be synergistically killed by the generated ROS and released Ag⁺.[22,23] However, with regard to in vivo antimicrobial application, the

Scheme 1. Schematical Illustration Showing the Synergistic Bacteria-Killing Behavior of Ag$^+$ and Photocatalytic Effects of ROS Produced by the Hybrid Ag$_3$PO$_4$/GO Coating Which Combines with Ti by PDA under Irradiation with 660 nm Visible Light Leading to Damage of the Bacterial Cell Membranes, Proteins, and DNA
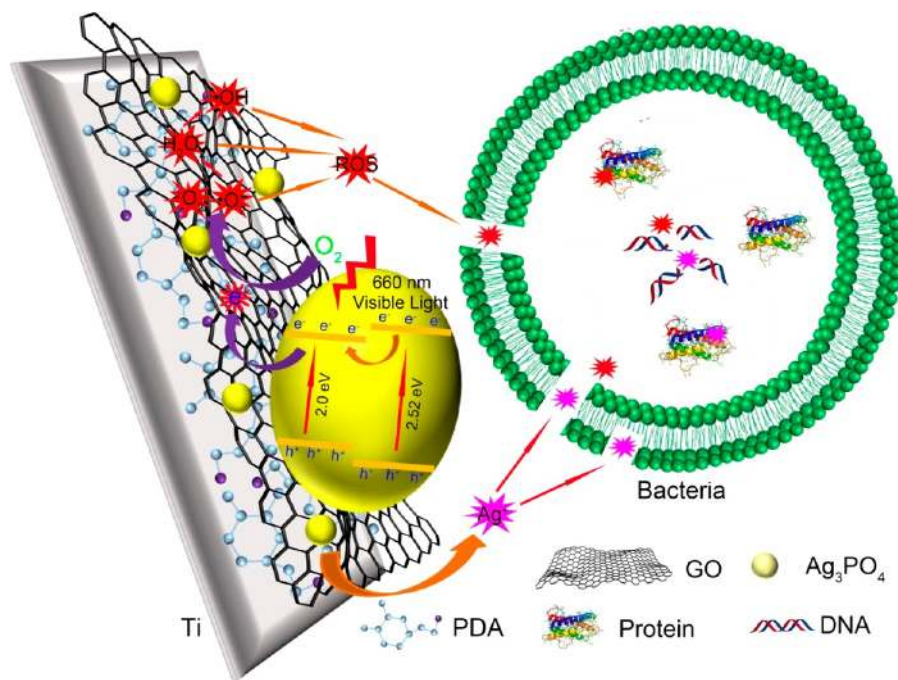
shortcoming is that it is difficult to control the release rate of Ag$^+$ and a high silver concentration is detrimental.[24,25] In addition, Ag$_3$PO$_4$ with a bandgap of 2.52 eV can only be excited by visible light that cannot readily penetrate human skin.[26] Therefore, it is necessary to find an appropriate carrier to load Ag$_3$PO$_4$ and tune the bandgap so that light with a longer wavelength can be used for in situ antimicrobial therapy. In this respect, graphene oxide (GO) is a desirable host to load nanoparticles due to the large specific surface area and oxygen-containing functional groups.[27] Owing to its excellent electrical conductivity, GO can mitigate recombination of photogenerated electron−hole pairs by rapid transfer of the electron−hole pairs from the photocatalyst to GO to enhance the photocatalytic properties.[28,29] GO has been utilized to adjust the bandgap of some semiconductor nanomaterials like ZnO and ZnS by forming chemical bonds at the interface between the nanoparticles (NPs) and GO sheets.[30,31] It has been shown that GO with oxygen-containing functional groups can chelate with Ag$^+$ to abate leaching of Ag$^+$ and reduce the cytotoxicity[32,33] thereby opening the possibility of long-term prevention of bacterial infection if Ag ions are released gradually from the Ag-containing coatings to the surroundings. At the same time, polydopamine (PDA) with excellent biocompatibility[34] also can reduce the cytotoxicity of Ag$^+$ and easily combine with other materials.[35]

Herein, we report a controllable, rapid, and efficient in situ disinfection technique by exploiting the synergistic actions of Ag$^+$ and ROS produced by Ag$_3$PO$_4$ under irradiation of 660 nm visible light by tuning the bandgap of the Ag$_3$PO$_4$ NPs using GO (Scheme 1). ROS increase the membrane permeability so that Ag$^+$ can enter the bacteria more easily, and thus both Ag$^+$ and ROS can destroy the DNA and proteins synergistically. In addition, PDA can be combined with a variety of materials, which means the strategy can be applicable to not only metallic implants such as Ti but also biopolymers like PEEK.

■ RESULTS AND DISCUSSION

Characterization of Ag$_3$PO$_4$/GO Nanofilm. The X-ray diffraction (XRD) patterns in Figure 1a show the typical (002) diffraction peak assigned to GO at $2\theta \approx 10°$[36] and peaks of Ag$_3$PO$_4$ at 2θ of 21°, 30°, 34°, 37°, 48°, 53°, 56°, and 58° from PDA/Ag$_3$PO$_4$-Ti confirming successful preparation of GO nanosheets and Ag$_3$PO$_4$ NPs on Ti. However, after Ag$_3$PO$_4$ combines with GO in either PDA/Ag$_3$PO$_4$/GO-Ti or PDA/Ag$_3$PO$_4$/GO-PEEK, the typical Ag$_3$PO$_4$ peaks still exist but that of GO disappears, indicating that Ag$_3$PO$_4$ NPs are incorporated into the GO nanosheets and the structure of GO is destroyed. Also, the width of the (110) peak obviously increases because the electrostatic adsorption of GO favors the uniform distribution of Ag$_3$PO$_4$ NPs, while for PDA/Ag$_3$PO$_4$-Ti, those Ag$_3$PO$_4$ NPs may aggregate with each other to form particles with a larger size. Transmission electron microscopy (TEM) results in Figure 1b of GO and Ag$_3$PO$_4$/GO-4 (according to the size of Ag$_3$PO$_4$, the samples are designated as Ag$_3$PO$_4$/GO-1 to -4) show that GO is a translucent sheet with many folds, thus favoring loading of NPs. As for Ag$_3$PO$_4$/GO-4, the Ag$_3$PO$_4$ NPs are homogeneously distributed on the surface of the GO sheets, and the average size of the nanodots is about 10 nm. According to Figure S1, the weight of GO accounts for 29.19% of Ag$_3$PO$_4$/GO-4, and H$_2$O accounts for 1.71%. So the weight of Ag$_3$PO$_4$ accounts for 69.1% of Ag$_3$PO$_4$/GO-4, and the mass ratio of Ag$_3$PO$_4$ and GO is 2.37:1 for Ag$_3$PO$_4$/GO-4. The encapsulating efficiency of the system is about 70.32% by mass. The SEM images of PDA/Ag$_3$PO$_4$/GO-Ti-4 (according to the size of Ag$_3$PO$_4$, the PDA/Ag$_3$PO$_4$/GO coatings on Ti are labeled PDA/Ag$_3$PO$_4$/GO-Ti-1 to -4) and PDA/Ag$_3$PO$_4$/GO-PEEK-4 (the PDA/Ag$_3$PO$_4$/GO-4 coating covered on PEEK surface) (Figure 1b) show that PDA/Ag$_3$PO$_4$/GO adheres to Ti or PEEK, and the Ag$_3$PO$_4$ NPs are homogeneously distributed. Figure S2a shows that the other PDA/Ag$_3$PO$_4$/GO-Ti samples contain Ag$_3$PO$_4$ NPs with sizes of about 150, 80, 40, and 10 nm.
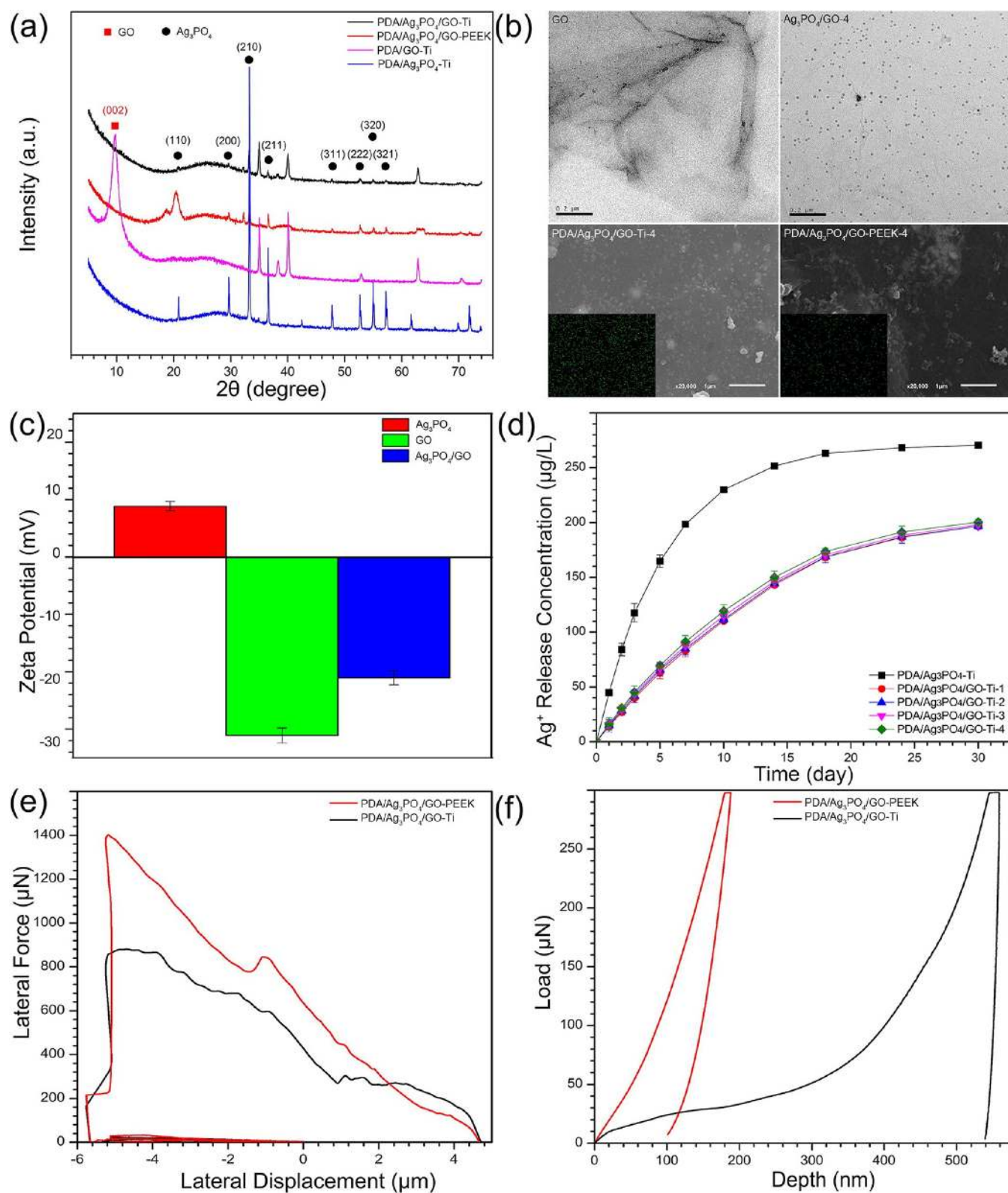
Figure 1. Structural and physical properties of Ag_3PO_4/GO. (a) XRD spectra of PDA/GO-Ti, PDA/Ag_3PO_4-Ti, PDA/Ag_3PO_4/GO-Ti, and PDA/Ag_3PO_4/GO-PEEK; (b) TEM images of GO and Ag_3PO_4/GO with the size of Ag_3PO_4 NPs being 10 nm and SEM images of PDA/Ag_3PO_4/GO-Ti and PDA/Ag_3PO_4/GO-PEEK together with the EDS data; (c) zeta potential of GO, Ag_3PO_4, as well as Ag_3PO_4/GO (0.347 mg/mL:0.0625 mg/mL). The error bars indicate means ± SD ($n = 3$); (d) Ag^+ release concentration profiles obtained by immersing five samples in 5 mL of neutral PBS at 37 °C. The error bars indicate means ± SD ($n = 3$); (e) force−displacement curve acquired by the nanoscratch test and (f) load−displacement curve by the nanoindentation test of PDA/Ag_3PO_4/GO-Ti and PDA/Ag_3PO_4/GO-PEEK to show the critical load and Young's modulus.
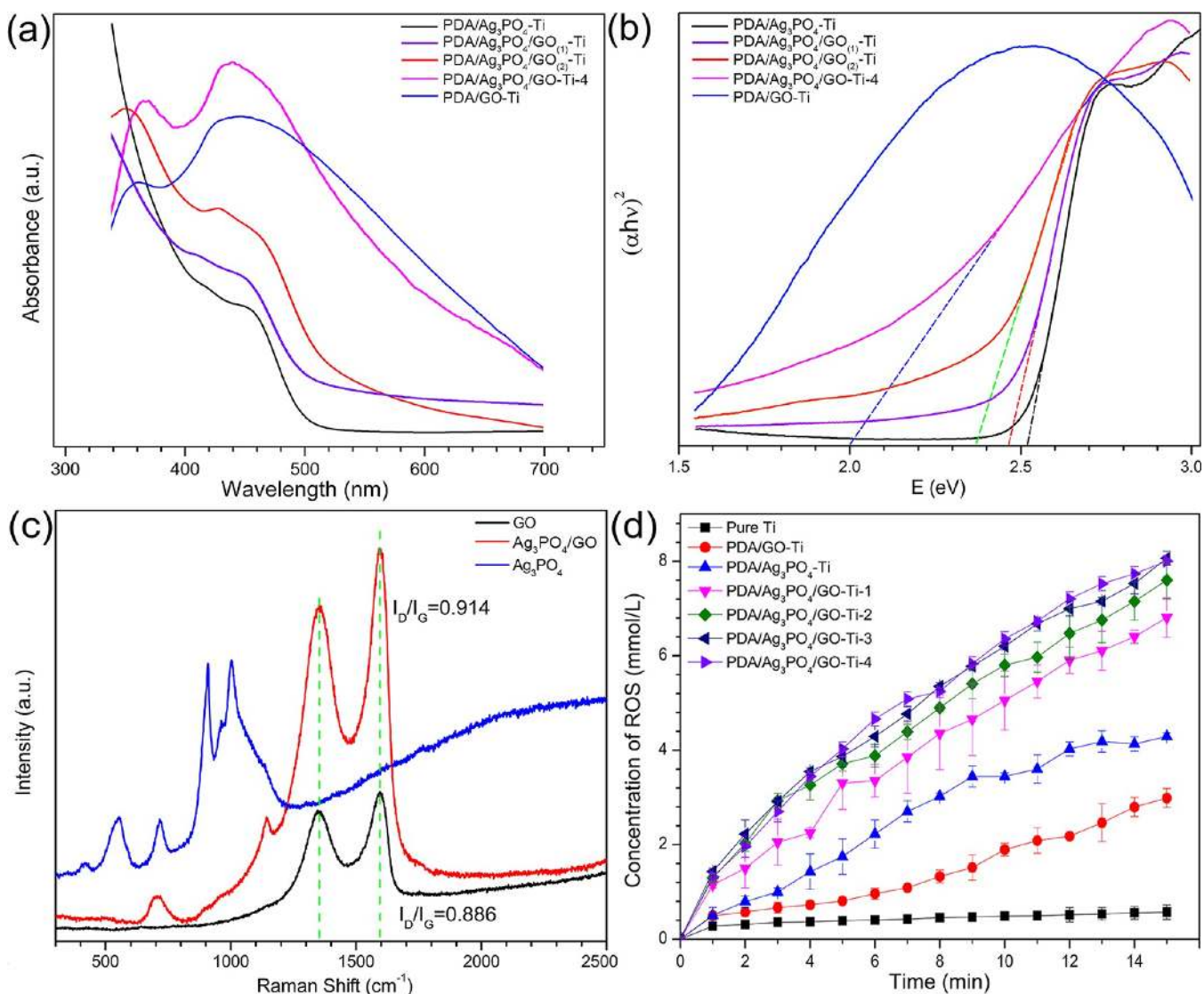
Figure 2. Photodynamic performance of Ag_3PO_4/GO. (a) Absorption wavelength and (b) corresponding bandgap of PDA/Ag_3PO_4-Ti, PDA/Ag_3PO_4/$GO_{(1)}$-Ti (Ag_3PO_4/GO = 41.86 mg/mL: 0.0625 mg/mL), PDA/Ag_3PO_4/$GO_{(2)}$-Ti (Ag_3PO_4/GO = 20.93 mg/mL: 0.0625 mg/mL), and PDA/Ag_3PO_4/GO-Ti-4; (c) Raman scattering spectra of GO, Ag_3PO_4, and Ag_3PO_4/GO; (d) ROS production curve of the samples after irradiation with 660 nm visible light for 15 min. The error bars indicate means $\pm$ SD (n = 3).

According to the zeta potential shown in Figure 1c, Ag_3PO_4 is positively charged, while GO is negatively charged. Hence, $Ag_3PO_4$ can easily bond with GO electrostatically, and the hybrid Ag_3PO_4/GO is negative. Moreover, PDA can combine with GO by intermolecular hydrogen bonds,[37] and the Ag_3PO_4/GO hybrid can be easily deposited on the surface of PDA-modified Ti substrate (sample designated as PDA/Ag_3PO_4/GO-Ti).

Although the released Ag^+ plays an important role in bacteria killing and prevention of bacterial infection,[38] excessive release of Ag^+ causes toxic effects.[39] Figure 1d shows that the PDA/Ag_3PO_4/GO-Ti samples exhibit the same Ag^+ release behavior regardless of the NPs size, and relatively stable release is observed in the initial 18 days. Subsequently, the release rate decreases, but Ag^+ could still be released even after nearly 30 days. The corresponding total concentration of Ag^+ is 251.01 μg/L, which was determined by inductively coupled plasma-atomic emission spectrometry (ICP-AES), much higher than those released from PDA/Ag_3PO_4/GO-Ti samples after immersion in PBS for 30 days, indicating that PDA/Ag_3PO_4/GO-Ti samples can provide a sustained Ag^+ release over 30 days. Compared with PDA/

Ag_3PO_4/GO-Ti, the PDA/Ag_3PO_4-Ti group exhibits a larger release of Ag^+ and accumulative Ag^+ concentration initially but almost no Ag^+ release after 18 days. The results suggest that GO mitigates the release of Ag^+ electrostatically. After immersion in PBS for one month, the surface morphology of PDA/Ag_3PO_4/GO-Ti changes only a little (Figure S2b), but the Ag signal detected by EDS decreases slightly due to the leaching of Ag from the coating surface, indicating that the hybrid nanofilm provides sustained Ag^+ release, thus boding well for long-term prevention of bacterial infection.

The thickness of the PDA/Ag_3PO_4/GO coating is about 500 nm according to the cross-sectional image and EDS mappings of Ag in Figure S2c. The binding force between the hybrid nanofilm of PDA/Ag_3PO_4/GO and substrate is determined by the nanoscratch tests (Figure 1e). The critical load is 0.9 mN, indicating that Ag_3PO_4/GO adheres well to the Ti substrate through PDA. The Young's modulus is 11 GPa (Figure 1f), which is similar to that of natural bone, thus reducing the stress shielding effect and rendering the materials more suitable for bone reconstruction than Ti and Ti alloys (55–110 GPa).[40,41]
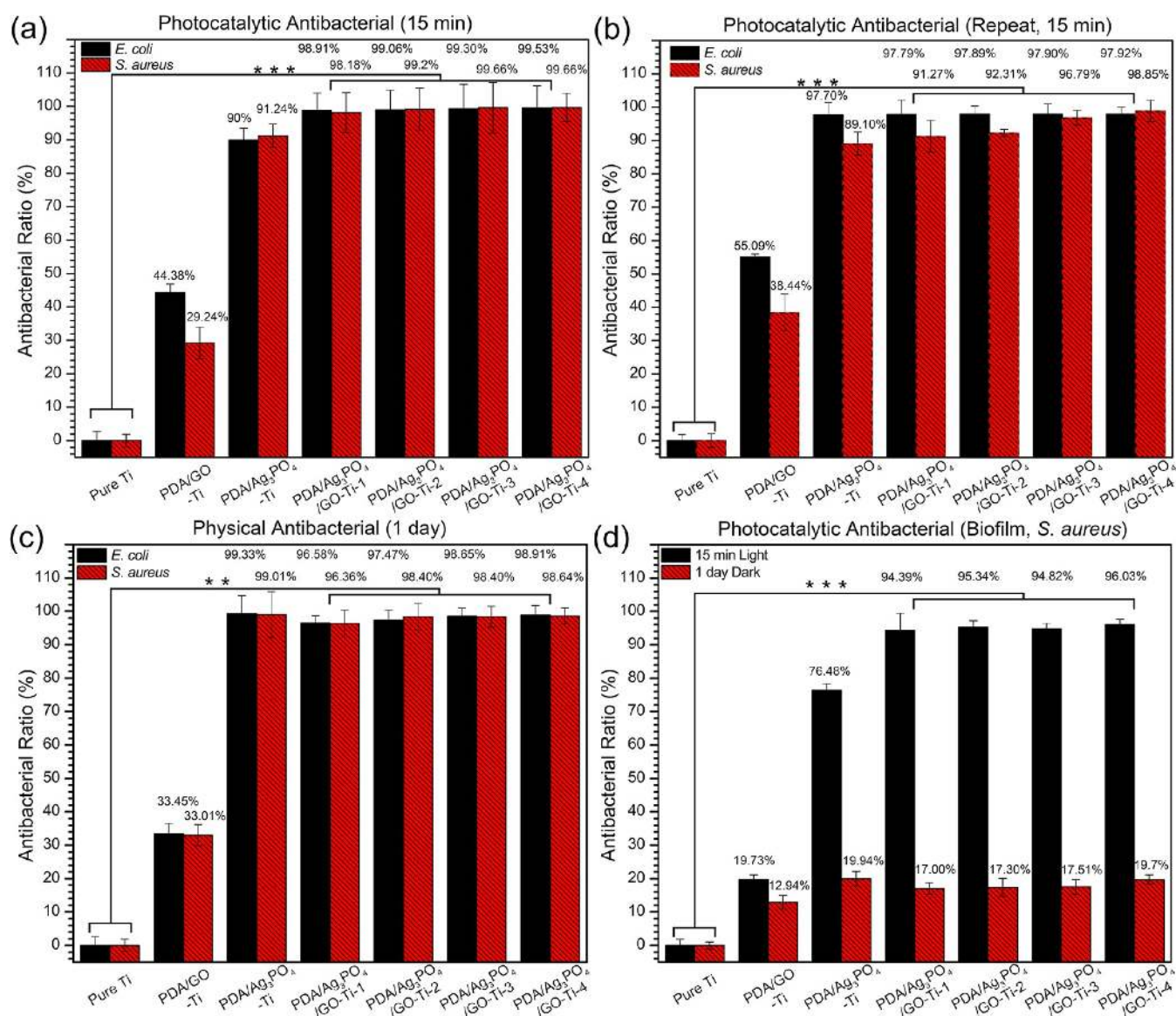
Figure 3. Antibacterial properties analysis. (a) Antibacterial ratio of the samples irradiated for 15 min with 660 nm visible light; (b) repeat photocatalytic antibacterial test for samples irradiated for 15 min with 660 nm visible light after the first photocatalytic antibacterial test and immersion in 10 mL of neutral PBS for 7 days; (c) physical antibacterial test for samples cocultured with bacteria for 1 day in the dark environment; (d) photocatalytic antibacterial test for samples with formed biofilms irradiated for 15 min with 660 nm visible light or cocultured for 1 day in the dark environment. The error bars indicate means $\pm$ SD ($n = 3$): *$p < 0.05$, **$p < 0.01$, ***$p < 0.001$, and all the experiments were done in triplicate.

Moreover, Ag_3PO_4/GO can be deposited on PDA-modified PEEK (Figure S2c). The critical load of 1.4 mN (Figure 1e) reveals good bonding strength between the nanofilm and PEEK and the Young's modulus of PDA/Ag_3PO_4/GO-PEEK is about 5 GPa (Figure 1f), which is also quite close to that of natural bone. Hence, PDA/Ag_3PO_4/GO can be applied onto both metallic and polymeric biomaterials.

Photocatalytic Properties. As shown in Figure 2a, PDA/GO-Ti does not exhibit characteristic absorption at wavelengths between 450 and 700 nm. The characteristic absorption wavelength of PDA/Ag_3PO_4-Ti is about 470 nm, which corresponds to the bandgap of 2.52 eV (Figure 2b).[42,43] Hence, Ag_3PO_4 does not have photocatalytic antimicrobial ability in vivo because 470 nm visible light cannot penetrate skin tissues. Therefore, it is necessary to adjust the absorption wavelength of Ag_3PO_4 to trigger the photocatalytic ability inside the body. After GO nanosheets are introduced, the absorption

wavelength is altered (Figure 2a). For example, the absorption wavelengths of PDA/Ag_3PO_4/$GO_{(1)}$-Ti (Ag_3PO_4/GO = 41.86 mg/mL:0.0625 mg/mL) and PDA/Ag_3PO_4/$GO_{(2)}$-Ti (Ag_3PO_4/GO = 20.93 mg/mL:0.0625 mg/mL) are 490 and 510 nm corresponding to bandgaps of 2.47 and 2.38 eV, respectively (Figure 2b). A larger GO ratio in Ag_3PO_4/GO is observed to red-shift the absorption wavelength of the Ag_3PO_4 NPs. When the ratio between Ag_3PO_4 and GO is 0.347 mg/mL: 0.0625 mg/mL (PDA/Ag_3PO_4/GO-Ti), the absorption wavelength shifts to about 660 nm, and the corresponding bandgap is reduced to 2.0 eV (Figure S3), which is not related to the size of Ag_3PO_4. This means that 660 nm visible light can trigger the photocatalytic activity of PDA/Ag_3PO_4/GO-Ti. The change can be ascribed to the structural change at the interface between Ag_3PO_4 and GO[44] as indicated by Raman scattering. As shown in Figure 2c, the Raman peaks of Ag_3PO_4 are at 560, 720, 930, and 1020 cm^{-1},[45] but the peaks from Ag_3PO_4 in Ag_3PO_4/GO-4
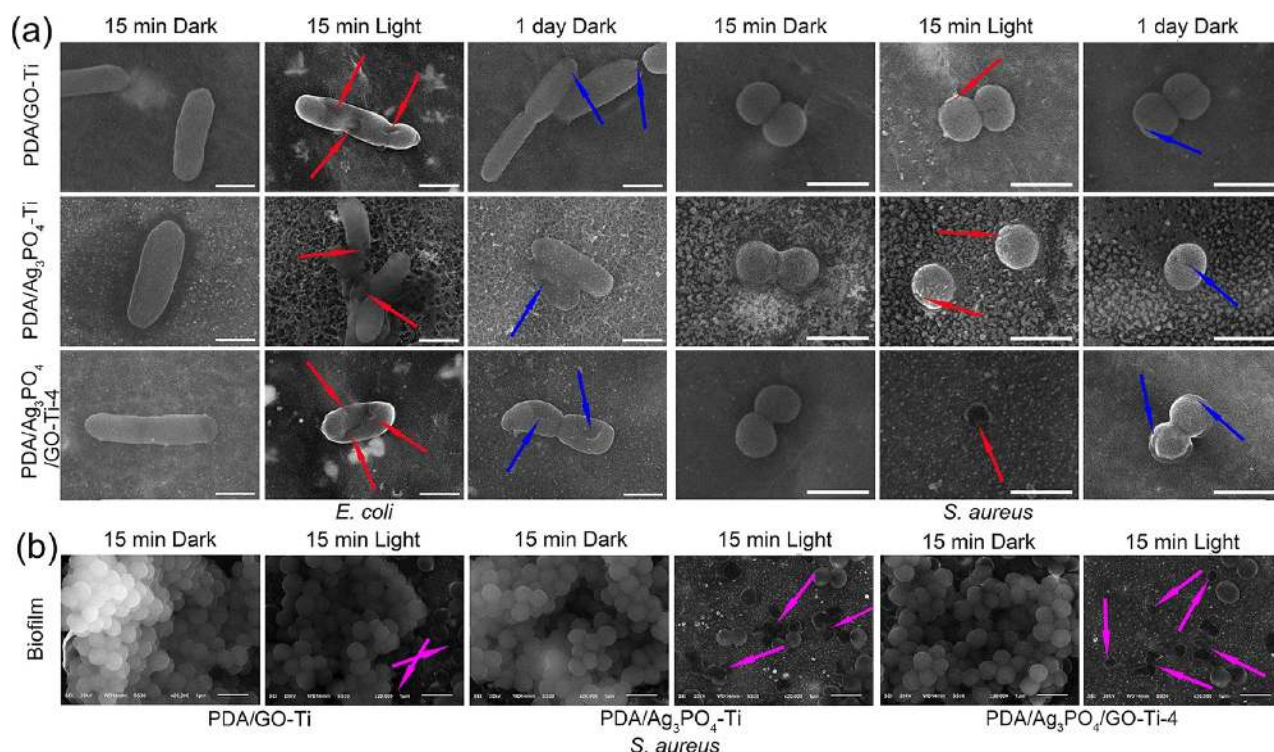
Figure 4. Surface morphology of the bacteria on the sample surface. (a) Intact bacterial membranes after culturing for 15 min in darkness versus shrunken or broken membranes (marked by red arrows for *E. coli* and blue arrows for *S. aureus*, respectively) after culturing for 1 day in darkness or irradiation for 15 min with 660 nm visible light; (b) SEM images of the biofilm formed on the samples after exposure to 660 nm visible light for 15 min or in darkness for 15 min (dead *S. aureus* marked by purple arrows). The scale bar is 1 μm. Each test was done in triplicate.

decrease significantly, suggesting that the structure of Ag_3PO_4 has changed after combining with GO. There are two characteristic peaks, one at 1350 cm^{-1} corresponding to the D band of sp^3 defects and the other at 1595 cm^{-1} associated with the G band of the sp^2 plane vibration in GO and Ag_3PO_4/GO-4.[46] The intensity ratio of the D band to G band (I_D/I_G) represents the ratio of defects. As shown in Figure 2c, I_D/I_G of GO is 0.886 and increases to 0.914 in Ag_3PO_4/GO-4 due to the strong interfacial interaction between GO and Ag_3PO_4 and change of sp^2 (C=C) to sp^3. Hence, according to the Raman results and Figure 1a, the structures of both Ag_3PO_4 and GO in Ag_3PO_4/GO-4 have changed with the formation of the Ag−O−C bond at the interface between the Ag_3PO_4 NPs and GO nanosheets. This also explains why the XRD peaks of GO disappear from PDA/Ag_3PO_4/GO-Ti (Figure 1a). The combination of GO nanosheets and Ag_3PO_4 NPs lowers the bottom of the conduction band of Ag_3PO_4 by facilitating interfacial electron transfer and electron−hole pair separation consequently reducing the bandgap of Ag_3PO_4. As a result, the photocatalytic activity of Ag_3PO_4/GO can be triggered by 660 nm visible light irradiation. Furthermore, previous studies have revealed that GO has the up-conversion photoluminescence (UCPL) ability to improve light absorption.[47−49] UCPL occurs when the photon energy of emission is higher than that of excitation (Figure S4).[50] Hence, GO may absorb 660 nm visible light (2.0 eV) to emit photons with higher energy (2.52 eV) to further enhance the photocatalytic activity of Ag_3PO_4.

ROS are produced from PDA/Ag_3PO_4/GO-Ti during 660 nm visible light irradiation to strengthen the antimicrobial effects.[51,52] Figure 2d shows the amounts of ROS generated from different samples. The PDA/Ag_3PO_4/GO-Ti series samples show higher ROS yields than either PDA/GO-Ti or

PDA/Ag_3PO_4−Ti, indicating that GO improves the photocatalytic activity of Ag_3PO_4 as discussed above. The ROS yields from PDA/Ag_3PO_4/GO-Ti decrease with increasing size of Ag_3PO_4 NPs because smaller Ag_3PO_4 has a larger specific surface area with more conduction electron oscillation[53] helping to absorb photons and produce more electrons. The electrons are transferred to the GO surface to produce ROS after contacting O_2 giving rise to better photocatalytic properties.

Antimicrobial Tests. As shown in the first-row image in Figure S5, the spread plate results indicate almost the same bacterial numbers of *Staphylococcus aureus* for all the groups in the dark for 15 min revealing no antimicrobial effects without light. In contrast, after exposure to 660 nm visible light for 15 min, the PDA/Ag_3PO_4/GO-Ti samples show decreased bacterial numbers, although the pure Ti group still shows the same results as those without light (second row in Figure S5). Hence, 660 nm visible light can stimulate the antimicrobial ability of Ag_3PO_4/GO but not pure Ti. The antimicrobial efficacy of the PDA/Ag_3PO_4/GO-Ti samples is higher than 98% (Figure 3a). Compared to PDA/Ag_3PO_4/GO-Ti, both the PDA/GO-Ti and PDA/Ag_3PO_4-Ti groups have much lower antimicrobial rates of 29.24% and 91.24%. These results are consistent with the ROS yields shown in Figure 2d, which discloses that 660 nm visible light irradiation stimulates Ag_3PO_4/GO to produce more ROS to kill bacteria with a better efficiency.[54,55] The results suggest that the hybrid of Ag_3PO_4 and GO has better photostimulated antimicrobial ability. As for the PDA/Ag_3PO_4/GO-Ti series samples, the amounts of *S. aureus* decrease gradually with decreasing Ag_3PO_4 size (Figure S5). The antimicrobial rates of PDA/Ag_3PO_4/GO-Ti-1, PDA/Ag_3PO_4/GO-Ti-2, PDA/Ag_3PO_4/GO-Ti-3, and PDA/Ag_3PO_4/GO-Ti-4 against *S. aureus* are 98.18%, 99.2%, 99.66%, and 99.66%,
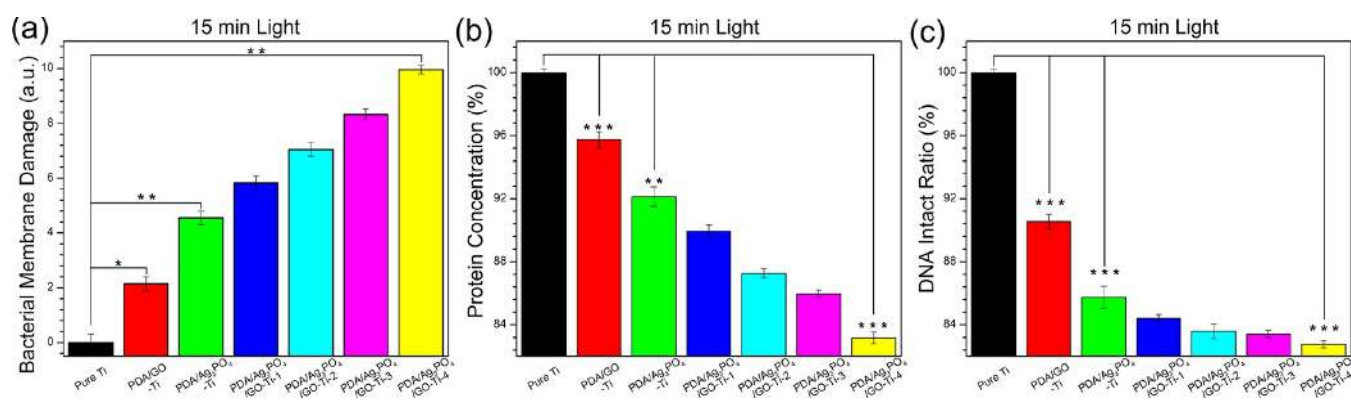
Figure 5. ROS damaging the membrane, protein, and DNA of bacteria. (a) Bacterial membrane damage histogram for bacteria cocultured with the samples and irradiated for 15 min with 660 nm visible light; (b) protein concentration histogram for the extracted bacteria protein after irradiation for 15 min with 660 nm visible light; (c) DNA intact ratio histogram of the extracted genomic DNA after irradiation for 15 min with by 660 nm visible light. The error bars indicate means ± SD ($n = 3$): *$p < 0.05$, **$p < 0.01$, ***$p < 0.001$.

respectively (Figure 3a), implying that the antimicrobial efficacy can be improved by reducing the size of the Ag_3PO_4 NPs and the corresponding higher yields of ROS (Figure 2d). In the case of *Escherichia coli*, it exhibits a similar trend, and the corresponding antibacterial efficacy is 98.91%, 99.06%, 99.30%, and 99.53% for $PDA/Ag_3PO_4/GO$-Ti-1, $PDA/Ag_3PO_4/GO$-Ti-2, $PDA/Ag_3PO_4/GO$-Ti-3, and $PDA/Ag_3PO_4/GO$-Ti-4, respectively. After the photodynamic antimicrobial test and subsequent immersion in PBS for 7 days, all the samples in the $PDA/Ag_3PO_4/GO$-Ti series show a repeatable antimicrobial rates over 97.79% and 91.27% against *E. coli* and *S. aureus*, respectively (Figure 3b), indicating that Ag_3PO_4/GO can produce repeatable and sustained photocatalytic antimicrobial effects. Compared to the first antimicrobial cycle, the photocatalytic antimicrobial activity of the Ag_3PO_4-based coatings diminishes slightly afterward due to release of Ag^+ after immersion in PBS for 7 days.

Although electrostatic adsorption between GO and Ag_3PO_4 makes Ag_3PO_4 more stable, Ag^+ is still slowly released (Figure 1d),[56] and both $PDA/Ag_3PO_4/GO$-Ti and PDA/Ag_3PO_4-Ti release Ag^+ to kill bacteria. As shown in Figure S5, after culturing for 1 day in darkness, both PDA/Ag_3PO_4-Ti and $PDA/Ag_3PO_4/GO$-Ti exhibit excellent antimicrobial activity against *S. aureus* with the former showing better antimicrobial efficiency because PDA/Ag_3PO_4-Ti can release more Ag^+ than $PDA/Ag_3PO_4/GO$-Ti due to electrostatic adsorption (Figure 1d). In the case of *E. coli*, spread plates test exhibit similar results (Figure S6). The physical antimicrobial rates of $PDA/Ag_3PO_4/GO$-Ti-4 are 98.91% and 98.64% against *E. coli* and *S. aureus*, respectively (Figure 3c).

Formation of biofilms is fatal to implants, and traditional treatment is usually not effective in removing biofilms.[57,58] As shown in Figure 3d and Figure S5, although Ag^+ leached from the coatings can kill bacteria efficiently after culturing for 1 day in darkness, it does not work for biofilms. The bacteria cultured from those peeled from the formed biofilm on samples by ultrasonic vibration spread on the samples after 1 day in the absence of light, and the antimicrobial rate is less than 20% (Figure 3d). After exposure to 660 nm visible light for 15 min, the amounts of bacteria on Ag_3PO_4 and Ag_3PO_4/GO decrease obviously, showing antimicrobial rates of over 94.39% against *S. aureus*, suggesting 660 nm light irradiation for a short time can break the biofilms on both PDA/Ag_3PO_4-Ti and $PDA/Ag_3PO_4/GO$-Ti. When the light exposure time is increased to 30 min, no

bacteria are observed (Figure S5), providing evidence that the biofilms are completely destroyed.

During light irradiation, the surface temperature of the samples rises inevitably (Figure S7a). The surface temperature quickly rises at first and then stays at a constant value below 44 °C during exposure for 15 min. The spread plate results in Figure S7b disclose that there is no difference between 45 and 37 °C for both *E. coli* and *S. aureus*, indicating that a temperature below 45 °C has no effects on the bacteria within 15 min.

Figure 4a shows the bacterial morphology on the different samples. For the three groups of samples in darkness for 15 min, both *E. coli* and *S. aureus* have the normal shape. In contrast, after irradiation for 15 min by 660 nm visible light, the two bacteria are deformed to different degrees as manifested by membrane damage for PDA/GO-Ti, PDA/Ag_3PO_4-Ti, and serious membrane shrinkage and cracking on $PDA/Ag_3PO_4/GO$-Ti (marked by red arrows). Although the membranes of the bacteria cultured in the dark for 1 day are also deformed to some extent due to the action of released Ag ions (marked by blue arrows), the damage is lower than that after 660 nm light irradiation for 15 min, indicating that photocatalytic antimicrobial activity of Ag_3PO_4/GO is more effective than that resulting from the released Ag ions. As shown in Figure 4b, the biofilms of *S. aureus* have almost the same morphology on the three kinds of samples in the dark for 15 min, indicating no antimicrobial activity. After irradiation with 660 nm light for 15 min, the biofilm still exists on the surface of PDA/GO-Ti with few dead bacteria (marked by pink arrows) but those on PDA/Ag_3PO_4-Ti and $PDA/Ag_3PO_4/GO$-Ti disappear as indicated by collapsed bacterial cells (marked by pink arrows). That is, PDA/GO-Ti cannot resist the formation of biofilms but those on PDA/Ag_3PO_4-Ti and $PDA/Ag_3PO_4/GO$-Ti are destroyed with the latter showing better results. These results are consistent with the spread plate results in Figure S5. The effects of the Ag_3PO_4 size on the bacterial morphology are shown in Figure S8. Similarly, the bacteria retain a normal shape in the dark for 15 min on all samples irrespective of particle size. After 660 nm light irradiation for 15 min, the deformation degree increases with decreasing particle size decreases due to the different yields of ROS (Figure 2d). Although bacterial deformation appears after culturing for 1 day in darkness, there is almost no difference because the amount of released Ag^+ is almost the same despite the Ag_3PO_4 size.

Antimicrobial Mechanism. ROS kill bacteria by destroying the cell membranes, proteins, and DNA.[59] The extent of damage
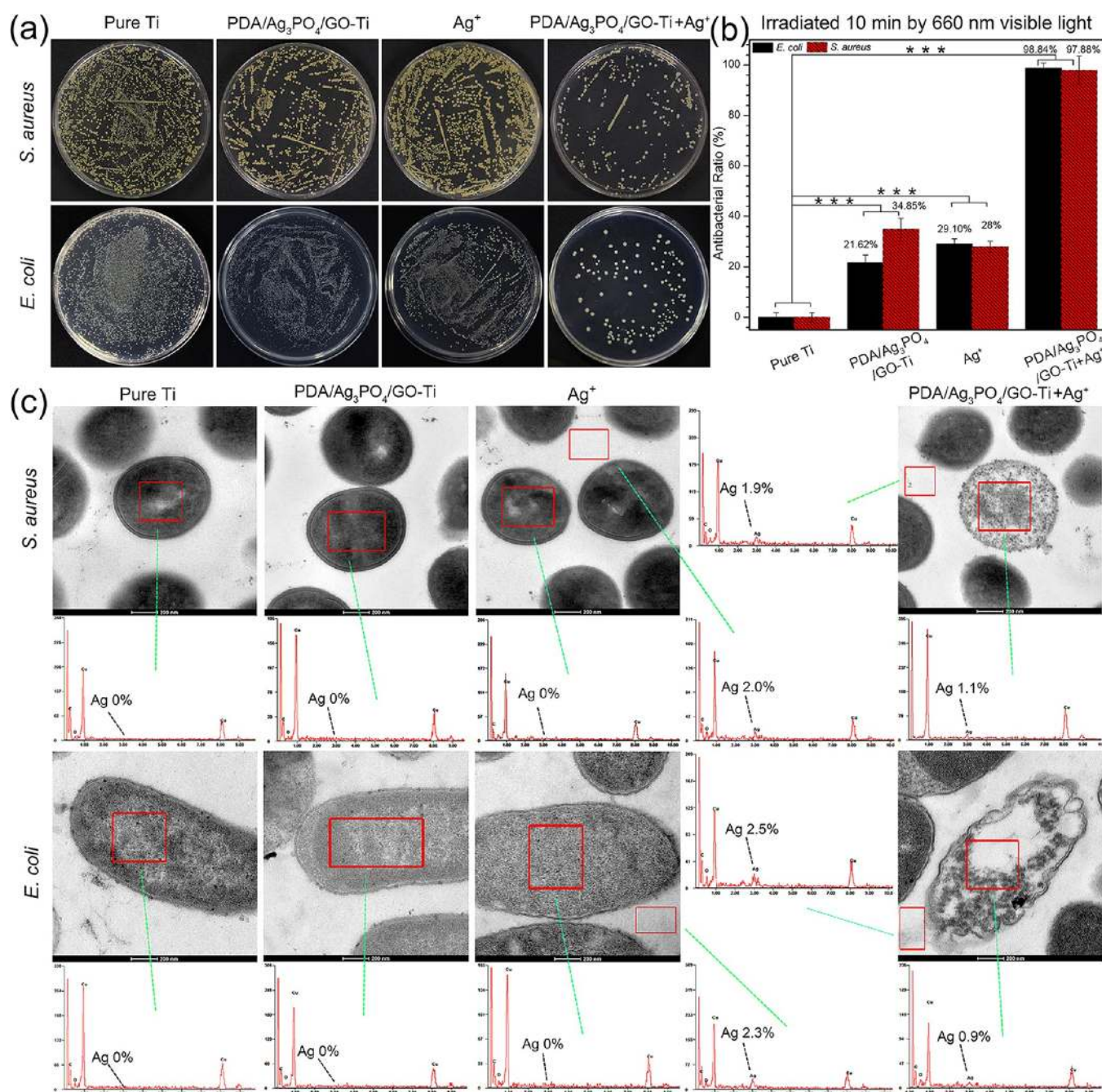
Figure 6. Synergistic antimicrobial effects of ROS and Ag^+. (a) Spread plate results of the bacteria cocultured with the samples (three samples for each group) after irradiation for 10 min with 660 nm visible light; (b) corresponding antimicrobial ratio histogram of (a). The error bars indicate means $\pm$ SD ($n = 3$): $*p < 0.05$, $**p < 0.01$, $***p < 0.001$; (c) TEM images of the bacterial sections and corresponding EDS patterns after coculturing with the samples and irradiation with 660 nm visible light for 10 min.

to the bacterial membrane can be determined by detecting the proteins leached from damaged bacterial cells. No protein is released from the intact bacteria during the centrifuge process, and a larger content of released protein means more damaged bacteria. The bacterial membrane damage rate is shown in Figure 5a. As for pure Ti group, it cannot destroy the bacterial membrane, so the amount of protein is defined as zero. Compared to the pure Ti group, damaged bacterial membrane for the other group is observed after irradiation for 15 min with 660 nm light, and the extent of damage varies with the ROS amounts produced from different samples, i.e., higher ROS yields producing more damage. For example, the most serious

membrane damage observed from $PDA/Ag_3PO_4/GO-Ti$ is caused by the highest ROS yield as shown in Figure 2d. After the bacterial membrane is broken, ROS destroys the intracellular proteins (Figure 5b) and DNA (Figure 5c). The bacterial proteins and genomic DNA are collected and detected by BCA protein assay kit (cat. no. P0010, Beyotime, China) and BIO-RAD (CFX Connect, Real-Time System). Pure Ti group also cannot destroy the proteins and genomic DNA, so it can be collected from the bacteria on the light-illuminated pure Ti group that are intact. But those sampled from the samples irradiated with 660 nm light show damage to a different degree. All in all, a
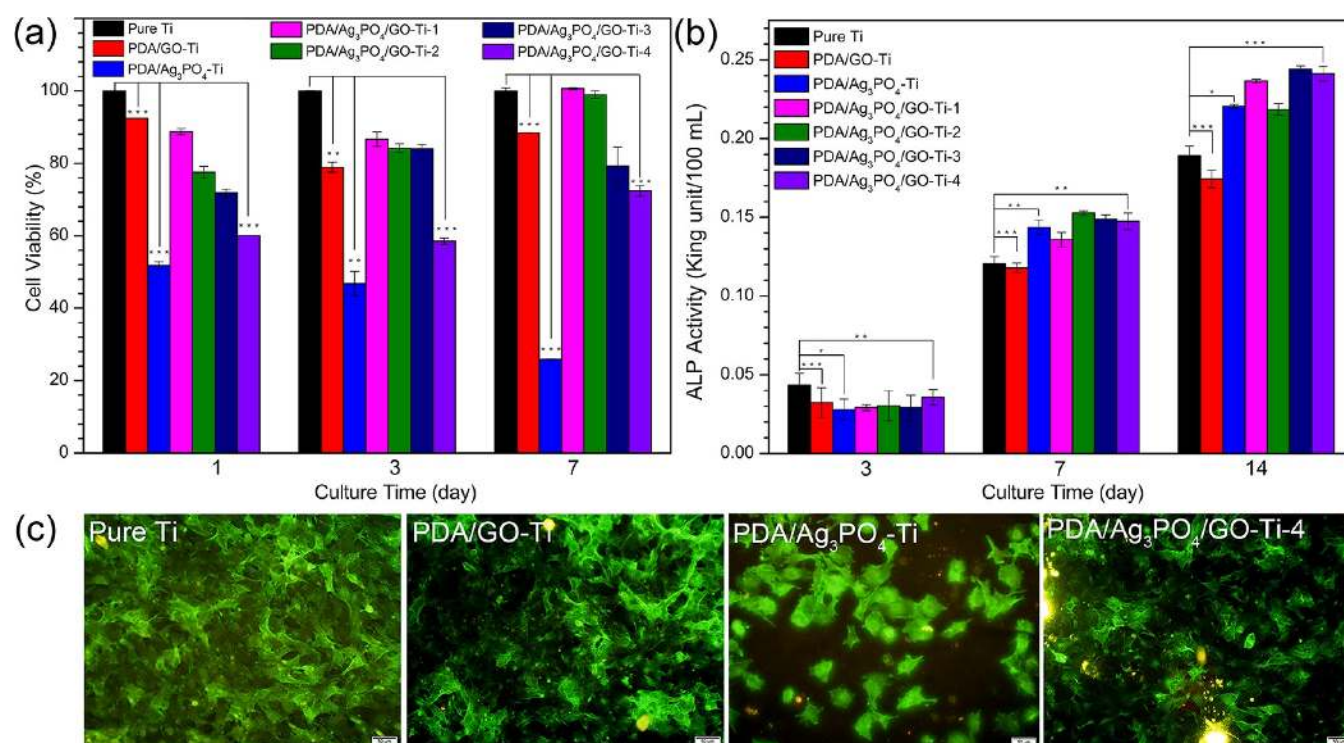
Figure 7. In vitro cytocompatibility. (a) MTT results showing the cell viability for cells cocultured with the samples in the dark. The error bars indicate means $\pm$ SD ($n = 3$): *$p < 0.05$, **$p < 0.01$, ***$p < 0.001$; (b) ALP activity showing the osteogenic differentiation of cells cultured on the samples in the dark. The error bars indicate means $\pm$ SD ($n = 3$): *$p < 0.05$, **$p < 0.01$, ***$p < 0.001$; (c) fluorescence micrographs for cells after culturing on the samples in the dark for 1 day (scale bar: 50 μm).

higher ROS yield produces more serious protein and DNA damage.

Synergistic bacteria killing by ROS and Ag$^+$. The spread plate and antibacterial ratio histogram in Figure 6a,b disclose that either PDA/Ag$_3$PO$_4$/GO-Ti or Ag$^+$ alone cannot kill most of the bacteria after irradiation for 10 min by 660 nm visible light. However, when Ag$^+$ and ROS are both present (PDA/Ag$_3$PO$_4$/GO-Ti + Ag$^+$), higher antimicrobial efficacy is achieved. According to our results, ROS produced in 10 min are not enough to kill most of the bacteria (Figure 6a,b). But ROS can change the permeability of the bacterial membranes (Figure 5a), which can be beneficial for Ag$^+$ entering into the inside of the bacteria. It can be proven by Figure 6c. The bacterial membranes on the light-irradiated Ti samples are intact and thick, and no Ag signal can be detected from inside the bacteria. The bacterial section images obtained from the light-irradiated PDA/Ag$_3$PO$_4$/GO-Ti and Ag$^+$ samples show the same morphology, and EDS cannot detect Ag from inside the bacteria. However, for the PDA/Ag$_3$PO$_4$/GO-Ti + Ag$^+$ group, the membranes of both *E. coli* and *S. aureus* are damaged almost completely, and EDS shows Ag penetration into the bacteria. These results confirm that ROS produced by PDA/Ag$_3$PO$_4$/GO-Ti after irradiation for 10 min by 660 nm visible light are insufficient to kill most of the bacteria, but with the aid of Ag$^+$ penetrating the membranes, they are killed within 10 min after the ROS damage the cell membranes. The Ag$^+$ entering the bacteria continue to destroy the membrane, intracellular proteins, and DNA to kill the bacteria. The large white space in the bacteria results from the leakage of damaged proteins and DNA.

In Vitro Cytocompatibility. The numbers of cells living on the surface of the samples represent the biocompatibility of the samples. As shown in Figure 7a, the PDA/Ag$_3$PO$_4$−Ti samples

show increasing cytotoxicity with the increase of culture time in darkness due to the highest concentration of Ag$^+$ released from the coating (Figure 1d). In contrast, the PDA/Ag$_3$PO$_4$/GO-Ti samples exhibit lower cytotoxicity due to the electrostatic adsorption between Ag$_3$PO$_4$ and GO. For example, after culturing for 1 day, the PDA/Ag$_3$PO$_4$/GO-Ti-1 sample exhibits the highest cell viability of 88%, while the viability of other groups is between 60 and 80% with the following order PDA/Ag$_3$PO$_4$/GO-Ti-2 > PDA/Ag$_3$PO$_4$/GO-Ti-3 > PDA/Ag$_3$PO$_4$/GO-Ti-4 because Ag$_3$PO$_4$ with a smaller size has a larger surface area that leads to relatively higher Ag$^+$ release concentration (Figure 1d), thus showing lower cell viability. However, as the culturing time increases, the cell viability of all PDA/Ag$_3$PO$_4$/GO-Ti samples is increased. After 7 days of culturing, the cell viability of both PDA/Ag$_3$PO$_4$/GO-Ti-1 and PDA/Ag$_3$PO$_4$/GO-Ti-2 is close to the level of pure Ti. Even for both PDA/Ag$_3$PO$_4$/GO-Ti-3 and PDA/Ag$_3$PO$_4$/GO-Ti-4, their cell viability is also enhanced and close to 80%. Besides the reduced releasing rate of Ag$^+$ as the culturing time increases, it has been reported that PDA can also increase biocompatibility.[37] In addition, the number of cells on the PDA/Ag$_3$PO$_4$/GO-Ti samples increases with cultured time because Ag$^+$ release diminishes with time. As shown in Figure 7b, after culturing for 7 and 14 days, all PDA/Ag$_3$PO$_4$/GO-Ti samples exhibit higher ALP activity compared to pure Ti, indicating the better osteogenetic ability of PDA/Ag$_3$PO$_4$/GO-Ti samples. Furthermore, Ag$_3$PO$_4$ can be partially decomposed to produce Ag,[20] which is favorable for the growth of osteoblasts by the microgalvanic effect between Ag and Ti.[60] In addition, the cell morphologies on those samples also do not change obviously (Figure 7c).

However, irradiation for 15 min under 660 nm visible light significantly weakens the cytocompatibility of PDA/Ag$_3$PO$_4$/
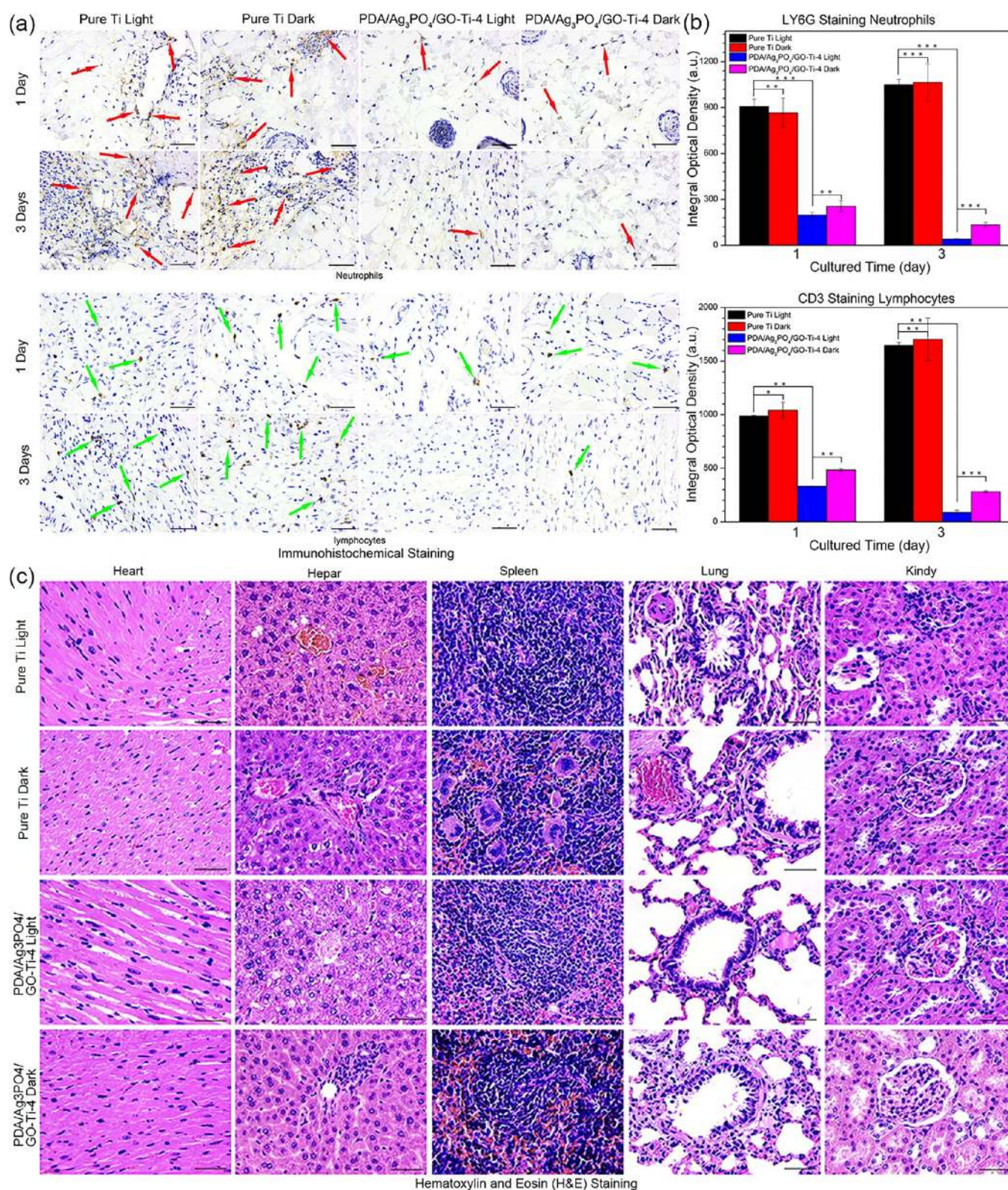
Figure 8. (a) Immunohistochemical staining for rat tissue slices of epidermal tissues in contact with the samples stained by LY6G for neutrophils and CD3 for lymphocytes. The neutrophils are marked by red arrows and lymphocytes are marked by green arrows; (b) integral optical density (IOD) histogram of neutrophils and lymphocytes, showing the amounts of immune cells, and larger values mean more immune cells. The error bars indicate means $\pm$ SD ($n = 3$): *$p < 0.05$, **$p < 0.01$, ***$p < 0.001$; (c) H&E staining of visceral tissue slices of rats after implantation for 3 days. The scale bar is 50 μm.

GO-Ti (Figure S9a), and as the irradiation time increases, the cytotoxicity becomes more pronounced (Figure S9b). It is believed that ROS is detrimental to cell proliferation, although it

does not mean that the cells cannot survive on the samples under light irradiation. As shown in Figure S9c, the cells can still survive on the Ag_3PO_4/GO coating, but compared with those shown in

Figure 7c, the cell numbers have been significantly reduced. In addition, since light irradiation occurs for a short time, the in vitro cell viability does not reflect the real in vivo tissue toxicity.

In Vivo Evaluation. The animal model of specific pathogen-free SD male rats are divided into two groups (pure Ti group and PDA/Ag_3PO_4/GO-Ti-4 group), and each group had four rats (half of the rats in each group are irradiated for 15 min with 660 nm visible light). The samples and 20 μL of *S. aureus* (1×10^7 CFU/mL^{-1}) are implanted into the subcutaneous tissues of the rats to build the animal model. These implanted rats are cultured for 1 day or 3 days. Once the animal model has a bacterial infection, the infected site produces immune cells such as neutrophils cells, lymphocytes, and so on. More bacteria in the tissues indicate more severe inflammatory response, resulting in more immune cells, which can also prove the poor antibacterial activity of the samples.

As shown in Figure 8a, the histological section by immunohistochemical staining of neutrophils and lymphocytes shows that the Ti group has many neutrophils (marked by red arrows) and lymphocytes (marked by the green arrows) in both 660 nm light irradiation for 15 min or in darkness groups. Moreover, as shown in Figure 8b (the immune cells integral optical density (IOD) histogram, larger values mean more immune cells), the immune cells are the same for 660 nm light irradiation for 15 min or in darkness groups, indicating that pure light irradiation has no effects on bacteria. In addition, the inflammation response becomes more serious in 3 days. But for the PDA/Ag_3PO_4/GO-Ti-4 group, only few neutrophils and lymphocytes occur, and the immune cells are decreased with the increase of culture time due to the photocatalytic antimicrobial efficacy of PDA/Ag_3PO_4/GO-Ti-4 irradiated by 660 nm light within a short time. In addition, even in darkness, this group can also exhibit a lower inflammatory response than the pure Ti group, indicating that the released Ag^+ from the coating can resist bacterial infection. These results confirm that PDA/Ag_3PO_4/GO-Ti-4 samples have not only excellent photocatalytic antibacterial activity but also physical antibacterial activity, which can be further proven by hematoxylin and eosin (H&E) staining (Figure S10a) and Giemsa staining results (Figure S10b).

It is noted that the released Ag^+ can circulate in the body, but according to the histological analysis of the heart, hepar, spleen, lung, and kidney of rats cultured for 3 days, no abnormal effects or damage are observed (Figure 8c), proving that the PDA/Ag_3PO_4/GO-Ti is safe in vivo.

■ CONCLUSIONS

PDA/Ag_3PO_4/GO coatings are suitable for biomedical implants due to the excellent antimicrobial ability and elastic modulus close to that of natural bone. They can also be deposited on both metallic and polymeric materials. GO improves the photo-dynamic performance of Ag_3PO_4 on account of the excellent electrical conductivity which mitigates recombination of photo-generated electron–hole pairs and accelerates electron transport to improve the photocatalytic performance of Ag_3PO_4. GO also alters the bandgap of Ag_3PO_4/GO so that the photodynamic antimicrobial ability can be achieved under 660 nm visible light illumination. The antimicrobial capability of the hybrid PDA/Ag_3PO_4/GO coatings increases with decreasing Ag_3PO_4 nano-particle size because a larger specific surface area leads to more effective release of Ag^+ and absorption of more photons to produce ROS. Ag^+ and ROS function synergistically to damage the DNA, proteins, and bacterial membranes, resulting in

bacteria death. The generated ROS change the permeability of the cell membranes, consequently allowing easier passage of Ag^+ into the bacteria cells to kill them.

■ METHODS

Synthesis of Ag_3PO_4/GO Composites. The GO powders, prepared by modified Hummer's method,[61,62] were dispersed in deionized (DI) water ultrasonically and 0.034 g of $AgNO_3$ was added to prepare four groups with different concentrations ($AgNO_3$/GO = 3.397 mg/mL:0.5 mg/mL, 1.699 mg/mL:0.25 mg/mL, 0.849 mg/mL:0.125 mg/mL, and 0.423 mg/mL:0.0625 mg/mL). After stirring for 30 min, 10 mL of 0.0067 mol/L Na_2HPO_4 were added dropwise to the mixture and the mixture was stirred vigorously for 30 min. Finally, the four groups were adjusted to the same concentration (Ag_3PO_4/GO = 0.347 mg/mL:0.0625 mg/mL).

Preparation of PDA/Ag_3PO_4/GO-Ti or PDA/Ag_3PO_4/GO-PEEK. After mechanical polishing with SiC, the biomedical Ti plates (Φ6 mm × 2.5 mm, Baosteel Group Corp, Shanghai China) were hydrothermally treated according to the procedures reported in our previous work.[63] A layer of PDA was prepared on the surface of Ti,[37] and the samples were immersed in the Ag_3PO_4/GO solutions with different particle size for 1 day under vacuum conditions and then washed with DI water. According to the size of Ag_3PO_4, the samples were labeled PDA/Ag_3PO_4/GO-Ti-1 to -4. Other samples which only had GO (0.0625 mg/mL) or Ag_3PO_4 (0.347 mg/mL) were named PDA/GO-Ti or PDA/Ag_3PO_4-Ti. The PDA/Ag_3PO_4/GO-PEEK samples underwent the same process without the hydrothermal treatment.

Characterization. Scanning electron microscopy (SEM, JSM-6510LV, JEOL, Japan) was used to examine the sample morphology and EDS; XRD showed the composition and phase. Nanoindentation was employed to assess the adhesion strength between the coatings and substrates. The amount of Ag^+ released was determined by inductively coupled plasma atomic emission spectrometry (ICP-AES, Optimal 8000, PE, USA). UV−visible spectrophotometry was performed on the UV-3600 (Shimadzu, Japan), and transmission electron microscopy (TEM, FEI, TF20, USA) was performed to examine the morphology. The cell morphology was observed under an inverted fluorescence microscope (IX73, Olympus, Japan).

Ag^+ Release Test. Five samples (PDA/Ag_3PO_4/GO-Ti-1 to -4 and PDA/Ag_3PO_4-Ti, five samples in each group) were immersed in 5 mL of PBS (pH = 7.4) at 37 °C, and the controlled-release solutions were taken out at intervals of 1, 2, 3, 5, 7, 10, 14, 18, 22, and 30 days. The solutions were refreshed each time, and the quantities of Ag^+ were determined by ICP-AES. In addition, five PDA/Ag_3PO_4/GO-Ti-4 samples were ultrasonically stripped to make Ag_3PO_4 completely free from the sample. The obtained solution was added with an excess of acid to completely dissolve the Ag_3PO_4, and the Ag^+ concentration was measured using ICP-AES.

ROS Test. The amount of ROS determined the antimicrobial capacity of the samples and was measured on a microplate reader using 10 mmol/L 2′,7′-dichlorofluorescein diacetate (DCFH-DA). Once DCFH-DA was combined with ROS, it can generate a fluorescent 2′,7′-dichlorofluorescein (DCF), which can be detected by a microplate reader. First, a microplate reader (the excitation wavelength is 488 to 525 nm) was used to measure the value of 100 μL of DCFH-DA reacted with excess ROS. Next, the samples (PDA/Ag_3PO_4/GO-Ti-1 to 4, PDA/Ag_3PO_4-Ti, PDA/GO-Ti, and pure Ti, three samples for each group, stored under dark conditions) were placed on 96-well plates, and 100 μL of the

capture agent were added to each well. The samples were irradiated for 15 min with 660 nm visible light from a laser with a power of 170 mW (MRL-III-660Dnm-500 mW-16090712, China). The liquid was measured every minute by the microplate reader. The yield of ROS was obtained by comparing the microplate reader values.

Antimicrobial Tests. The antimicrobial effects of the samples were assessed based on the ROS and Ag^+ antimicrobial behavior. They were evaluated by spread plate and SEM. Two types of bacteria, *E. coli* and *S. aureus* (1×10^7 colony-forming units per milliliter (CFU/mL)), were used. The samples were stored in darkness and sterilized with alcohol and ultraviolet light before the experiments. All the experiments were done in triplicate for better statistics.

In the spread plate test, 8 mL of sterile solid agar Luria-Bertain (LB) media were poured into each plate and 20 μL of the bacterial liquid and 20 μL of PBS (pH = 7.4) were taken out to be evenly poured onto each plate. Afterward, the plates were cultured for 1 day at 37 °C and the number of colonies on the plates was recorded on a digital camera. If the plates had no colonies, the spread plate process was repeated again with 200 μL of the bacterial liquid. The number of colonies was recorded using the photos of the spread plate and the antimicrobial ratio was calculated using the following equation (N = number of colonies):

$$\text{bactericidal ratio (\%)} = (N_{\text{control}} - N_{\text{sample}})/N_{\text{control}}$$

After the antimicrobial test, the bacteria were loaded on the samples that were immersed in 200 μL of 2.5% glutaraldehyde for 2 h and washed three times with PBS. The samples were dehydrated with alcohol (30%, 50%, 70%, 90%, and 100%) for 15 min each and after drying, the bacterial morphology was observed by SEM.

The samples and 100 μL of the bacteria liquid (*E. coli* or *S. aureus*) were added to 96-well plate and irradiated for 15 min with 660 nm visible light. The bacteria liquid was diluted one hundred times for the spread plate as the first photocatalytic antimicrobial test. The samples were collated again and immersed in PBS (pH = 7.4) at 37 °C for 7 days. Afterward, the samples are used to repeat the above antimicrobial test in the repeat photocatalytic antimicrobial test.

To assess formation of biofilms, the samples and 200 μL of bacteria liquid (*S. aureus* 1×10^8 CFU/mL) were added to 96-well plates and cultured for 2 days at 37 °C. The bacteria liquid was changed every 12 h and afterward, the bacteria biofilm formed on the surface of samples. The samples and 100 μL of PBS (pH = 7.4) were poured onto new plates and irradiated for 15 min with 660 nm visible light or cultured in dark for 1 day. The bacteria were then collected and diluted 50 000 times for the spread plate test. Three antimicrobial tests were performed and the bacterial morphology was observed by SEM.

To evaluate the Ag^+ antimicrobial behavior, the samples and 100 μL of the bacteria liquid (*E. coli* or *S. aureus*) were added to 96-well plates. The samples were cultured for 15 min or 1 day in a dark environment at 37 °C. Afterward, the bacteria liquid was diluted a hundred times for the spread plate test. The bacterial morphology was observed and the samples with formed biofilms underwent the spread plate test after culturing for 1 day.

Antimicrobial Mechanism. The samples and 100 μL of bacteria liquid (*S. aureus*) were added to 96-well plates and irradiated for 15 min with 660 nm visible light. The bacterial liquid was collected, centrifuged, and taken out to determine the

protein concentration by BCA Protein Assay Kit (cat# P0010, Beyotime, China). All the experiments were done in triplicate.

To assess the role of ROS, 3 mL of the bacteria liquid (*S. aureus*) were crushed to exposure the protein completely. The samples and 100 μL of the bacteria liquid were added to 96-well plates and irradiated for 15 min with 660 nm visible light. The protein concentration in the liquid was determined by the BCA Protein Assay Kit.

The bacteria DNA was extracted using the bacteria DNA kit (Feiyang, Guangzhou, China). 100 μL of the extracted DNA liquid and samples were added to 96-well plates and irradiated for 15 min with 660 nm visible light. The DNA liquid was collected and the DNA concentration was measured on the BIO-RAD CFX Connect Real-Time System.

ROS and Ag^+ Synergistic Antimicrobial Effect. Six PDA/Ag_3PO_4/GO-Ti-4 samples and 200 μL PBS are added into 96-well plates. After placed at 37 °C for 2 days' release of Ag^+, the PBS solution that contains Ag^+ is collected. Next, four groups (pure Ti or PDA/Ag_3PO_4/GO-Ti-4 + 100 μL 1×10^7 CFU/mL bacterial liquid, and PDA/Ag_3PO_4/GO-Ti-4 or blank well + 90 μL PBS contained Ag^+ + 10 μL 1×10^8 CFU/mL bacterial liquid, each group sets three parallel samples) are irradiated 10 min by 660 nm visible light. And then the bacterial liquid is collected for spread plate. And the test is repeated five times, the bacteria are collected to make bacterial slices,[64] and observed by TEM.

In Vitro Tests. The biological activity was evaluated by 3-[4,5-dimethylthiazol-2-yl]-2,5-diphenyl tetrazolium bromide (MTT) and cell morphology observation. The MC3T3-E1 cells (mouse calvarial cell line) were obtained from Tongji Hospital, Wuhan, China. The samples were sterilized with 75% alcohol and then exposed to UV for 30 min and stored under dark condition. All the experiments were done in triplicate.

In the MTT test, the samples and 200 μL of the cell liquid (1×10^4 cells/mL cells) were added into 96-well plates, each sample was set to three parallel groups. After incubation for 1, 3, and 7 days at 37 °C in a 5% CO_2 incubator, 200 μL of the MTT solution with a concentration of 0.5 g/L (dissolved MTT powder into pH = 7.4 PBS solution) were dropped onto each well after removing the stock solution and cultured for 4 h. Finally, the liquid was taken out to measure the OD_{490} or OD_{570} on a microplate reader. The cytocompatibility of samples under three kinds of conditions, namely, in the dark, 660 nm light irradiation for 15 min, and 660 nm light irradiation for 20 min, was evaluated by the aforementioned MTT process.

To evaluate the cell morphology, the samples and 100 mL of the cell liquid (1×10^3 cells/mL cell) were added to 96-well plates. Each sample was set to two parallel groups, and one group of each was irradiated for 15 min with 660 nm visible light. After incubation for 1 day at 37 °C in a 5% CO_2 incubator, the cells were dyed by FITC (100 nM YiSen, Shanghai) as described previously.[65] After drying, the cell morphology was examined by inverted fluorescence microscope.

In Vivo Tests. The specific pathogen-free SD male rats (Hubei Provincial Centers for Disease Prevention & Control, 180 g) were cultured in quarantine for acclimatization and detection for 1 week to build a subcutaneous infection model. All the animal experiments and procedures were approved by Hubei Provincial Centers for Disease Prevention & Control. The rats were divided into two groups (pure Ti group and PDA/Ag_3PO_4/GO-Ti-4 group) and each group had 4 rats (half of the rats in each group were irradiated for 15 min with 660 nm visible light). The samples were implanted into the subcutaneous tissue of the rats together with 20 μL of *S. aureus* (1×10^7 CFU/mL^{-1}). After

1 and 3 days, the tissues in contact with the samples were collected to make tissue sections (immunohistochemical staining of neutrophils and lymphocytes, H&E staining, and Giemsa staining) to observe bacterial infection. The amounts of neutrophils and lymphocytes were calculated by IOD value, and larger values represent more neutrophils or lymphocytes. The viscera of the rats cultured for 3 days were collected to make tissue sections to observe the effects of samples for viscera.

■ STATISTICAL ANALYSIS

All the experiments data were analyzed by the one-way ANOVA and expressed as means ± standard deviations with $n = 3$. p values < 0.05 were considered statistically significant.

■ ASSOCIATED CONTENT

Ⓢ Supporting Information

The Supporting Information is available free of charge on the ACS Publications website at DOI: 10.1021/acscentsci.8b00177.

> Figures S1−10. TG curves of Ag_3PO_4/GO-4 (S1); structure analysis of GO/Ag_3PO_4 composites and Ag_3PO_4/GO-Ti (S2); absorption wavelength and corresponding bandgap of Ag_3PO_4/GO-Ti (S3); schematic image of up-conversion photoluminescence of Ag_3PO_4/GO (S4); spread plate results of *S. aureus* (S5); spread plate results of *E. coli* (S6); temperature change and corresponding spread plate (S7); bacterial morphology of *E. coli* and *S. aureus* (S8); in vitro evaluation (S9); in vivo evaluation (S10) (PDF)

■ AUTHOR INFORMATION

Corresponding Author

*E-mail: shuilin.wu@gmail.com; shuilinwu@tju.edu.cn.

ORCID Ⓘ

Yufeng Zheng: 0000-0002-7402-9979
Shuilin Wu: 0000-0002-1270-1870

Notes

The authors declare no competing financial interest.

■ ACKNOWLEDGMENTS

■ REFERENCES

(1) Jaggessar, A.; Shahali, H.; Mathew, A.; Yarlagadda, P. K. D. V. Bio-Mimicking Nano and Micro-Structured Surface Fabrication for Antimicrobial Properties in Medical Implants. *J. Nanobiotechnol.* 2017, 15, 64.

(2) Huo, S. D.; Jiang, Y.; Gupta, A.; Jiang, Z. W.; Landis, R. F.; Hou, S. Y.; Liang, X. J.; Rotello, V. M. Fully Zwitterionic Nanoparticle Antimicrobial Agents through Tuning of Core Size and Ligand Structure. *ACS Nano* 2016, 10, 8732−8737.

(3) He, X. J.; Zhang, X. G.; Wang, X.; Qin, L. Review of Antimicrobial Activity of Titanium-Based Implants' Surfaces Fabricated by Micro-Arc Oxidation. *Coatings* 2017, 7, 45.

(4) Bradley, P.; Gordon, N. C.; Walker, T. M.; Dunn, L.; Heys, S.; Huang, B.; Earle, S.; Pankhurst, L. J.; Anson, L.; de Cesare, M. D.; Piazza, P.; Votintseva, A. A.; Golubchik, T.; Wilson, D. J.; Wyllie, D. H.; Diel, R.; Niemann, S.; Feuerriegel, S.; Kohl, T. A.; Ismail, N.; Omar, S. V.; Smith, E. G.; Buck, D.; McVean, G. M.; Walker, A. S.; Peto, T. E. A.; Crook, D. W.; Iqbal, Z. Rapid Antibiotic-Resistance Predictions from Genome Sequence Data for Staphylococcus Aureus and Mycobacterium Tuberculosis. *Nat. Commun.* 2016, 7, 11465.

(5) Zhao, Z. W.; Yan, R.; Yi, X.; Li, J. L.; Rao, J. M.; Guo, Z. Q.; Yang, Y. M.; Li, W. F.; Li, Y. Q.; Chen, C. Y. Bacteria-Activated Theranostic Nanoprobes Against Methicillin-Resistant *Staphylococcus aureus* Infection. *ACS Nano* 2017, 11, 4428−4438.

(6) Tian, J. X.; Zhang, J. Y.; Yang, J. T.; Du, L. Y.; Geng, H.; Cheng, Y. Q. Conjugated Polymers Act Synergistically with Antibiotics to Combat Bacterial Drug Resistance. *ACS Appl. Mater. Interfaces* 2017, 9, 18512−18520.

(7) Pan, P. C.; Yu, H. D.; Liu, Q. L.; Kong, X. T.; Chen, H.; Chen, J. A.; Liu, Q.; Li, D.; Kang, Y.; Sun, H. Y.; Zhou, W. F.; Tian, S.; Cui, S. L.; Zhu, F.; Li, Y. Y.; Huang, Y.; Hou, T. J. Combating Drug-Resistant Mutants of Anaplastic Lymphoma Kinase with Potent and Selective Type-I-1/2 Inhibitors by Stabilizing Unique DFG-Shifted Loop Conformation. *ACS Cent. Sci.* 2017, 3, 1208−1220.

(8) Chen, W. Y.; Chang, H. Y.; Lu, J. K.; Huang, Y. C.; Harroun, S. G.; Tseng, Y. T.; Li, Y. J.; Huang, C. C.; Chang, H. T. Self-Assembly of Antimicrobial Peptides on Gold Nanodots: Against Multidrug-Resistant Bacteria and Wound-Healing Application. *Adv. Funct. Mater.* 2015, 25, 7189−7199.

(9) Holmbeck, M. A.; Shadel, G. S. Mitochondria Provide a 'Complex' Solution to a Bacterial Problem. *Nat. Immunol.* 2016, 17, 1009−1010.

(10) Zheng, K. Y.; Setyawati, M. I.; Lim, T. P.; Leong, D. T.; Xie, J. P. Antimicrobial Cluster Bombs: Silver Nanoclusters Packed with Daptomycin. *ACS Nano* 2016, 10, 7934−7942.

(11) Ji, D. K.; Zhang, Y.; Zang, Y.; Li, J.; Chen, G. R.; He, X. P.; Tian, H. Targeted Intracellular Production of Reactive Oxygen Species by a 2D Molybdenum Disulfide Glycosheet. *Adv. Mater.* 2016, 28, 9356−9363.

(12) Natan, M.; Gutman, O.; Lavi, R.; Margel, S.; Banin, E. Killing Mechanism of Stable N-Halamine Cross-Linked Polymethacrylamide Nanoparticles that Selectively Target Bacteria. *ACS Nano* 2015, 9, 1175−1188.

(13) Deng, C. H.; Gong, J. L.; Zhang, P.; Zeng, G. M.; Song, B.; Liu, H. Y. Preparation of Melamine Sponge Decorated with Silver Nano-particles-Modified Graphene for Water Disinfection. *J. Colloid Interface Sci.* 2017, 488, 26−38.

(14) Kawasaki, H.; Kumar, S.; Li, G.; Zeng, C. J.; Kauffman, D. R.; Yoshimoto, J.; Iwasaki, Y.; Jin, R. C. Generation of Singlet Oxygen by Photoexcited $Au_{25}(SR)_{18}$ Clusters. *Chem. Mater.* 2014, 26, 2777−2788.

(15) Ge, J. C.; Lan, M. H.; Zhou, B. J.; Liu, W. M.; Guo, L.; Wang, H.; Jia, Q. Y.; Niu, G.; Huang, X.; Zhou, H. Y.; Meng, X. M.; Wang, P. F.; Lee, C. S.; Zhang, W. J.; Han, X. D. A Graphene Quantum Dot Photodynamic Therapy Agent with High Singlet Oxygen Generation. *Nat. Commun.* 2014, 5, 4596.

(16) Cho, S. J.; Kim, S. Y.; Park, S. J.; Song, N.; Kwon, H. Y.; Kang, N. Y.; Moon, S. H.; Chang, Y. T.; Cha, H. J. Photodynamic Approach for Teratoma-Free Pluripotent Stem Cell Therapy Using CDy1 and Visible Light. *ACS Cent. Sci.* 2016, 2, 604−607.

(17) Chen, Z. H.; Bing, F.; Liu, Q.; Zhang, Z. G.; Fang, X. M. Novel Z-Scheme Visible-Light-Driven Ag_3PO_4/Ag/SiC Photocatalysts with Enhanced Photocatalytic Activity. *J. Mater. Chem. A* 2015, 3, 4652−4658.

(18) Zheng, B. J.; Wang, X.; Liu, C.; Tan, K.; Xie, Z. X.; Zheng, L. High-Efficiently Visible Light-Responsive Photocatalysts: Ag_3PO_4 Tetrahedral Microcrystals with Exposed {111} Facets of High Surface Energy. *J. Mater. Chem. A* 2013, 1, 12635−12640.

(19) Xu, J. W.; Gao, Z. D.; Han, K.; Liu, Y. M.; Song, Y. Y. Synthesis of Magnetically Separable Ag_3PO_4/TiO_2/Fe_3O_4 Heterostructure with Enhanced Photocatalytic Performance under Visible Light for Photo-inactivation of Bacteria. *ACS Appl. Mater. Interfaces* 2014, 6, 15122−15131.

(20) Deng, C. H.; Gong, J. L.; Ma, L. L.; Zeng, G. M.; Song, B.; Zhang, P.; Huan, S. Y. Synthesis, Characterization and Antimicrobial Perform-

ance of Visible Light-Responsive Ag_3PO_4 Particles Deposited on Graphene Nanosheets. *Process Saf. Environ. Prot.* **2017**, *106*, 246−255.

(21) Cao, J.; Luo, B. D.; Lin, H. L.; Xu, B. Y.; Chen, S. F. Visible Light Photocatalytic Activity Enhancement and Mechanism of $AgBr/Ag_3PO_4$ Hybrids for Degradation of Methyl Orange. *J. Hazard. Mater.* **2012**, *217-218*, 107−115.

(22) Yang, Z. M.; Huang, G. F.; Huang, W. Q.; Wei, J. M.; Yan, X. G.; Liu, Y. Y.; Jiao, C.; Wan, Z.; Pan, A. Novel Ag_3PO_4/CeO_2 Composite with High Efficiency and Stability for Photocatalytic Applications. *J. Mater. Chem. A* **2014**, *2*, 1750−1756.

(23) Yu, C. L.; Wei, L. F.; Chen, J. C.; Zhou, W. Q.; Fan, Q. Z.; Yu, J. Novel $AgCl/Ag_2CO_3$ Heterostructured Photocatalysts with Enhanced Photocatalytic Performance. *Rare Met.* **2016**, *35*, 475−480.

(24) Wang, T. T.; Liu, X. M.; Zhu, Y. Z.; Cui, Z. D.; Yang, X. J.; Pan, H. B.; Yeung, K. W. K.; Wu, S. L. Metal Ion Coordination Polymer-Capped pH-Triggered Drug Release System on Titania Nanotubes for Enhancing Self-Antimicrobial Capability of Ti Implants. *ACS Biomater. Sci. Eng.* **2017**, *3*, 816−825.

(25) Yu, W. Z.; Zhang, Y. Z.; Liu, X. M.; Xiang, Y. M.; Li, Z. Y.; Wu, S. L. Synergistic Antimicrobial Activity of Multi Components in Lysozyme/Chitosan/Silver/Hydroxyapatite Hybrid Coating. *Mater. Des.* **2018**, *139*, 351−362.

(26) Frontistis, Z.; Antonopoulou, M.; Petala, A.; Venieri, D.; Konstantinou, I.; Kondarides, D. I.; Mantzavinos, D. Photodegradation of Ethyl Paraben Using Simulated Solar Radiation and Ag_3PO_4 Photocatalyst. *J. Hazard. Mater.* **2017**, *323*, 478−488.

(27) Zhu, Y. W.; Murali, S.; Cai, W. W.; Li, X. S.; Suk, J. W.; Potts, J. R.; Ruoff, R. S. Graphene and Graphene Oxide: Synthesis, Properties, and Applications. *Adv. Mater.* **2010**, *22*, 3906−3924.

(28) Pan, Z. H.; Hisatomi, T.; Wang, Q.; Chen, S. S.; Iwase, A.; Nakabayashi, M.; Shibata, N.; Takata, T.; Katayama, M.; Minegishi, T.; Kudo, A.; Domen, K. Photoreduced Graphene Oxide as a Conductive Binder to Improve the Water Splitting Activity of Photocatalyst Sheets. *Adv. Funct. Mater.* **2016**, *26*, 7011−7019.

(29) Bu, Y. Y.; Chen, Z. Y. Role of Polyaniline on the Photocatalytic Degradation and Stability Performance of the Polyaniline/Silver/Silver Phosphate Composite under Visible Light. *ACS Appl. Mater. Interfaces* **2014**, *6*, 17589−17598.

(30) Liu, X. Q.; Yang, J. B.; Zhao, W.; Wang, Y.; Li, Z.; Lin, Z. Q. A Simple Route to Reduced Graphene Oxide-Draped Nanocomposites with Markedly Enhanced Visible-Light Photocatalytic Performance. *Small* **2016**, *12*, 4077−4085.

(31) Zhang, Y.; Zhang, N.; Tang, Z. R.; Xu, Y. J. Graphene Transforms Wide Band Gap ZnS to a Visible Light Photocatalyst. The New Role of Graphene as a Macromolecular Photosensitizer. *ACS Nano* **2012**, *6*, 9777−9789.

(32) Zeng, X. K.; McCarthy, D. T.; Deletic, A.; Zhang, X. W. Silver/Reduced Graphene Oxide Hydrogel as Novel Bactericidal Filter for Point-of-Use Water Disinfection. *Adv. Funct. Mater.* **2015**, *25*, 4344−4351.

(33) Shao, W.; Liu, X. F.; Min, H. H.; Dong, G. H.; Feng, Q. Y.; Zuo, S. L. Preparation, Characterization, and Antimicrobial Activity of Silver Nanoparticle-Decorated Graphene Oxide Nanocomposite. *ACS Appl. Mater. Interfaces* **2015**, *7*, 6966−6973.

(34) Huang, Y.; Li, Y. W.; Hu, Z. Y.; Yue, X. J.; Proetto, M. T.; Jones, Y.; Gianneschi, N. C. Mimicking Melanosomes: Polydopamine Nanoparticles as Artificial Microparasols. *ACS Cent. Sci.* **2017**, *3*, 564−569.

(35) Ding, X.; Liu, J. H.; Liu, D. P.; Li, J. Q.; Wang, F.; Li, L. J.; Wang, Y. H.; Song, S. Y.; Zhang, H. J. Multifunctional Core/Satellite Polydopamine@Nd^{3+}-Sensitized Upconversion Nanocomposite: A Single 808 nm Near-Infrared Light-Triggered Theranostic Platform for In Vivo Imaging-Guided Photothermal Therapy. *Nano Res.* **2017**, *10* (10), 3434−3446.

(36) Mao, C. Y.; Xiang, Y. M.; Liu, X. M.; Cui, Z. D.; Yang, X. J.; Yeung, K. W. K.; Pan, H. B.; Wang, X. B.; Chu, P. K.; Wu, S. L. Photo-Inspired Antimicrobial Activity and Wound Healing Acceleration by Hydrogel Embedded with Ag/Ag@AgCl/ZnO Nanostructures. *ACS Nano* **2017**, *11*, 9010−9021.

(37) Xie, X. Z.; Mao, C. Y.; Liu, X. M.; Zhang, Y. Z.; Cui, Z. D.; Yang, X. J.; Yeung, K. W. K.; Pan, H. B.; Chu, P. K.; Wu, S. L. Synergistic Bacteria Killing through Photodynamic and Physical Actions of Graphene Oxide/Ag/Collagen Coating. *ACS Appl. Mater. Interfaces* **2017**, *9*, 26417−26428.

(38) AshaRani, P. V.; Mun, G. L. K.; Hande, M. P.; Valiyaveettil, S. Cytotoxicity and Genotoxicity of Silver Nanoparticles in Human Cells. *ACS Nano* **2009**, *3*, 279−290.

(39) Geetha, M.; Singh, A. K.; Asokamani, R.; Gogia, A. K. Ti Based Biomaterials, the Ultimate Choice for Orthopaedic Implants. *Prog. Mater. Sci.* **2009**, *54*, 397−425.

(40) Biesiekierski, A.; Wang, J.; Gepreel, M. A. H.; Wen, C. A New Look at Biomedical Ti-Based Shape Memory Alloys. *Acta Biomater.* **2012**, *8*, 1661−1669.

(41) Li, J. Q.; Yuan, H.; Zhu, Z. F. In Situ Growth of Ag_3PO_4 on N-$BiPO_4$ Nanorod: A Core-Shell Heterostructure for High Performance Photocatalyst. *J. Colloid Interface Sci.* **2016**, *462*, 382−388.

(42) Wei, L.; Karahan, H. E.; Zhai, S. L.; Liu, H. W.; Chen, X. C.; Zhou, Z.; Lei, Y. J.; Liu, Z. W.; Chen, Y. Amorphous Bimetallic Oxide-Graphene Hybrids as Bifunctional Oxygen Electrocatalysts for Rechargeable Zn-Air Batteries. *Adv. Mater.* **2017**, *29*, 1701410.

(43) Chen, Q. Y.; Wang, Y. F.; Wang, Y. W.; Zhang, X. C.; Duan, D. H.; Fan, C. M. Nitrogen-Doped Carbon Quantum Dots/Ag_3PO_4 Complex Photocatalysts with Enhanced Visible Light Driven Photocatalytic Activity and Stability. *J. Colloid Interface Sci.* **2017**, *491*, 238−245.

(44) Chen, Y.; Dong, X. J.; Cao, Y.; Xiang, J. J.; Gao, H. Y. Enhanced Photocatalytic Activities of Low-Bandgap TiO_2-Reduced Graphene Oxide Nanocomposites. *J. Nanopart. Res.* **2017**, *19*, 200.

(45) Yang, X. F.; Cui, H. Y.; Li, Y.; Qin, J. L.; Zhang, R. X.; Tang, H. Fabrication of Ag_3PO_4-Graphene Composites with Highly Efficient and Stable Visible Light Photocatalytic Performance. *ACS Catal.* **2013**, *3*, 363−369.

(46) Cai, T.; Liu, Y. T.; Wang, L. L.; Zhang, S. Q.; Zeng, Y. X.; Yuan, J. L.; Ma, J. H.; Dong, W. Y.; Liu, C. B.; Luo, S. L. Silver Phosphate-Based Z-Scheme Photocatalytic System with Superior Sunlight Photocatalytic Activities and Anti-Photocorrosion Performance. *Appl. Catal., B* **2017**, *208*, 1−13.

(47) Liu, F.; Jang, M. H.; Ha, H. D.; Kim, J. H.; Cho, Y. H.; Seo, T. S. Facile Synthetic Method for Pristine Graphene Quantum Dots and Graphene Oxide Quantum Dots: Origin of Blue and Green Luminescence. *Adv. Mater.* **2013**, *25*, 3657−3662.

(48) Gan, Z. X.; Wu, X. L.; Zhou, G. X.; Shen, J. C.; Chu, P. K. Is There Real Upconversion Photoluminescence from Graphene Quantum Dots? *Adv. Opt. Mater.* **2013**, *1*, 554−558.

(49) Zhu, S. J.; Song, Y. B.; Zhao, X. H.; Shao, J. R.; Zhang, J. H.; Yang, B. The Photoluminescence Mechanism in Carbon Dots (Graphene Quantum Dots, Carbon Nanodots, and Polymer Dots): Current State and Future Perspective. *Nano Res.* **2015**, *8*, 355−381.

(50) Ha, H. D.; Jang, M. H.; Liu, F.; Cho, Y. H.; Seo, T. S. Upconversion Photoluminescent Metal Ion Sensors Via Two Photon Absorption in Graphene Oxide Quantum Qots. *Carbon* **2015**, *81*, 367−375.

(51) Cai, Y. C.; Li, C. L.; Wu, D.; Wang, W.; Tan, F. T.; Wang, X. Y.; Wong, P. K.; Qiao, X. L. Highly Active MgO Nanoparticles for Simultaneous Bacterial Inactivation and Heavy Metal Removal from Aqueous Solution. *Chem. Eng. J.* **2017**, *312*, 158−166.

(52) Sirelkhatim, A.; Mahmud, S.; Seeni, A.; Kaus, N. H. M.; Ann, L. C.; Bakhori, S. K. M.; Hasan, H.; Mohamad, D. Review on Zinc Oxide Nanoparticles: Antimicrobial Activity and Toxicity Mechanism. *Nano-Micro Lett.* **2015**, *7*, 219−242.

(53) Sun, Y. G.; Xia, Y. N. Gold and Silver Nanoparticles: A Class of Chromophores with Colors Tunable in the Range from 400 to 750 nm. *Analyst* **2003**, *128*, 686−691.

(54) Hao, Y. J.; Liu, B.; Tian, L. J.; Li, F. T.; Ren, J.; Liu, S. J.; Liu, Y.; Zhao, J.; Wang, X. J. Synthesis of {111} Facet-Exposed MgO with Surface Oxygen Vacancies for ROS Generation in the Dark. *ACS Appl. Mater. Interfaces* **2017**, *9*, 12687−12693.

(55) Rasool, K.; Helal, M.; Ali, A.; Ren, C. E.; Gogotsi, Y.; Mahmoud, K. A. Antimicrobial Activity of Ti$_3$C$_2$Tx Mxene. *ACS Nano* **2016**, *10*, 3674−3684.

(56) Xu, Z. Q.; Li, M.; Li, X.; Liu, X. M.; Ma, F.; Wu, S. L.; Yeung, K. W. K.; Han, Y.; Chu, P. K. Antimicrobial Activity of Silver Doped Titanate Nanowires on Ti Implants. *ACS Appl. Mater. Interfaces* **2016**, *8*, 16584−16594.

(57) Liu, Y.; Busscher, H. J.; Zhao, B. G.; Li, Y. F.; Zhang, Z. K.; van der Mei, H. C.; Ren, Y. J.; Shi, L. Q. Surface-Adaptive, Antimicrobially Loaded, Micellar Nanocarriers with Enhanced Penetration and Killing Efficiency in Staphylococcal Biofilms. *ACS Nano* **2016**, *10*, 4779−4789.

(58) Duncan, B.; Li, X. N.; Landis, R. F.; Kim, S. T.; Gupta, A.; Wang, L. S.; Ramanathan, R.; Tang, R.; Boerth, J. A.; Rotello, V. M. Nanoparticle-Stabilized Capsules for the Treatment of Bacterial Biofilms. *ACS Nano* **2015**, *9*, 7775−7782.

(59) Gehring, J.; Trepka, B.; Klinkenberg, N.; Bronner, H.; Schleheck, D.; Polarz, S. Sunlight-Triggered Nanoparticle Synergy: Teamwork of Reactive Oxygen Species and Nitric Oxide Released from Mesoporous Organosilica with Advanced Antimicrobial Activity. *J. Am. Chem. Soc.* **2016**, *138*, 3076−3084.

(60) Jin, G. D.; Qin, H.; Cao, H. L.; Qian, S.; Zhao, Y. C.; Peng, X. C.; Zhang, X. L.; Liu, X. Y.; Chu, P. K. Synergistic Effects of Dual Zn/Ag Ion Implantation in Osteogenic Activity and Antibacterial Ability of Titanium. *Biomaterials* **2014**, *35*, 7699−7713.

(61) Li, R. B.; Mansukhani, N. D.; Guiney, L. M.; Ji, Z. X.; Zhao, Y. C.; Chang, C. H.; French, C. T.; Miller, J. F.; Hersam, M. C.; Nel, A. E.; Xia, T. Identification and Optimization of Carbon Radicals on Hydrated Graphene Oxide for Ubiquitous Antimicrobial Coatings. *ACS Nano* **2016**, *10*, 10966−10980.

(62) Giuri, A.; Masi, S.; Colella, S.; Kovtun, A.; Dell'Elce, S.; Treossi, E.; Liscio, A.; Corcione, C. E.; Rizzo, A.; Listorti, A. Cooperative Effect of GO and Glucose on PEDOT:PSS for High VOC and Hysteresis-Free Solution-Processed Perovskite Solar Cells. *Adv. Funct. Mater.* **2016**, *26*, 6985−6994.

(63) Liu, Z. H.; Zhu, Y. Z.; Liu, X. M.; Yeung, K. W. K.; Wu, S. L. Construction of Poly(Vinyl Alcohol)/Poly(Lactide-Glycolideacid)/Vancomycin Nanoparticles on Titanium for Enhancing the Surface Self-Antimicrobial Activity and Cytocompatibility. *Colloids Surf., B* **2017**, *151*, 165−177.

(64) Li, J.; Tan, L.; Liu, X. M.; Cui, Z. D.; Yang, X. J.; Yeung, K. W. K.; Chu, P. K.; Wu, S. L. Balancing Bacteria-Osteoblast Competition through Selective Physical Puncture and Biofunctionalization of ZnO/Polydopamine/Arginine-Glycine-Aspartic Acid-Cysteine Nanorods. *ACS Nano* **2017**, *11*, 11250−11263.

(65) Lin, S.; Liu, X. M.; Tan, L.; Cui, Z. D.; Yang, X. J.; Yeung, K. W. K.; Pan, H. B.; Wu, S. L. Porous Iron-Carboxylate Metal-Organic Framework: A Novel Bioplatform with Sustained Antimicrobial Efficacy and Nontoxicity. *ACS Appl. Mater. Interfaces* **2017**, *9*, 19248−19257.